Heat transfer characteristics of thermally and hydrodynamically developing flows in multi-layer mini-channel heat sinks

H. Nemati[1,*], M.A. Moghimi[2], C.N. Markides[3,4]

[1] Department of Mechanics, Marvdasht Branch, Islamic Azad University, Marvdasht, Iran
[2] Department of Design and Engineering, Staffordshire University, Stoke-On-Trent ST4 2DE, UK
[3] Clean Energy Processes (CEP) Laboratory, Department of Chemical Engineering, Imperial College London, South Kensington Campus, London SW7 2AZ, UK
[4] Kutateladze Institute of Thermophysics, Siberian Branch of the Russian Academy of Sciences, Russian Federation

* Corresponding author: H.Nemati@miau.ac.ir

Abstract

In this study, a novel type of air-cooled heat sink is proposed, which consists of several layers of mini-channels. In this design, the hydraulic diameter is smaller than in conventional types of heat sinks, such as plate-fin heat sinks, and consequently, the achievable heat transfer rates are higher. To predict the cooling performance of this heat sink, an innovative analytical method is proposed, results from which are complemented by an extensive number of numerical simulations of the simultaneously developing flows, thermally and hydrodynamically, inside a rectangular channel of the heat sink. The results of the analytical method are compared against two- and three-dimensional simulations and good agreement is found, while from the simulations, correlations are proposed for the Nusselt number in these flows. Finally, the performance of the proposed heat sink is compared to a plate-fin heat sink. This comparison reveals that entropy generation in the latter is around 27% higher than in the former, and suggests a promising advantage of the proposed heat sink design.

Keywords: developing flow, heat sink, mini-channel, multi-layer, rectangular channel.

Nomenclature

A	Area [m^2]
A_c	channels cross-section area [m^2]
c_P	Constant pressure specific heat capacity [J/kg.K]
D_h	Channel hydraulic diameter [m]
f	Friction factor
h	Heat transfer coefficient [W/m^2.K]
k_f	Air thermal conductivity [W/m.K]
k_s	Heat sink thermal conductivity [W/m.K]
L	Channel length [m]
L_f	Heat sink length [m]
$\dot{m}$	Air mass flow rate [kg/s]

N	Number of rows
Nu	Nusselt number
$\overline{Nu}$	Average Nusselt number
P	Pressure [Pa]
$\mathcal{P}$	Channel wetted perimeter [m]
$Pr = \frac{\mu c_P}{k_\mathrm{f}}$	Prandtl number
q	Total heat flux [W]
q''	Heat flux per unit area [W/m^2]
R	Air gas constant [J/kg.K]
$Re = \frac{\rho U_\mathrm{in} W}{\mu}$	Reynolds number
s	Specific entropy [J/kg.K]
T	Temperature [K]
t	Thickness [m]
U	Total heat transfer coefficient [W/K]
$\overline{U}$	Air average velocity [m/s]
U_in	Inlet air velocity [m/s]
$\vec{V}$	Velocity vector [m/s]
V_z	Velocity component along channel length [m/s]
W	Channel width [m]
x, y, z	Cartesian coordinate system

Greek letters

ΔP	Pressure drop [Pa]
Δs	Entropy change [J/kg.K]
$\theta = T - T_\infty$	Temperature difference [K]
μ	Viscosity [Pa.s]
ρ	Air density [kg/m^3]

Subscripts

amb	Ambient
b	Base
eff	Effective
eq	Equivalent
I	Primary fin

II	Secondary fin
in	Inlet
m	Mean
out	Outlet
w	Wall
∞	Based on the inlet temperature

1. Introduction

Temperature control in precision electronic devices is one of the major challenges for the further advancement of this technology, and this challenge is being exacerbated by the rapid development of microelectronics. Plate-fin heat sinks are one of the most commonly used heat sink types in the electronics industry for keeping the temperature below a critical limit. Despite their simplicity and benefits, their performance is not high enough to cover all requirements. Several attempts have been made to increase the performance of plate-fin heat sinks by utilizing various methods such as entropy generation minimization [1] or constructal law [2]. Despite these efforts, higher cooling rates are still demanded in recent technological developments. This demand may be met using two-phase flow [3-5] or microchannel liquid-cooling heat sinks that can increase the heat transfer rate close to 800 W/m^2. However, this heat transfer rate can only be accessible at the expense of a considerable pressure drop of around 200 kPa. Such high pressure drop penalty in the microchannel was reported by many researchers [6-9] using mini-channels with a characteristic length of 0.2 to 3 mm is more beneficial.

Gao et al. [10] conducted experimental studies on demineralised water in microchannels and proved that two-dimensional channels with a height greater than 0.4 mm can be treated by the usual thermal and hydraulic rules. Reynaud et al. [11] reported that measured heat transfer and friction coefficients for water flow in mini-channels match with the conventional correlations. Nemati et al. [12] optimised the mini-channel by the combination of MOGA (Multi-Objective Genetic Algorithm) and LINMAP (Linear Programming Technique for Multidimensional Analysis of Preference) methods and proposed to disturb slightly the cross-section of the second-half of the channel length which decreases overall thermal resistance by 87% with only 10% increases in pumping power. Al-Rashed et al. [13] studied the effects of using a biologically synthesized water-silver nano-fluid on hydrothermal performance and irreversibility in a wavy microchannel heat sink. They showed increasing the nano additives fraction increases the convective heat transfer coefficient and consequently reduces the CPU surface temperature. They also showed that in the wavy channel increasing the wave amplitude reduces the rate of entropy generation by about 69 % but increasing the wavelength increases the entropy generation rate by about 44% which is an adverse effect.

In all the aforementioned investigations and many other studies, only one array of channels with water as coolant was investigated. The high thermal capacity of water and its availability besides its low price have made it an interesting coolant choice. However, several technical and practical issues including the piping requirement, leakage problems, sedimentation, and so on, promote using air as cooling media in studies. Air is a non-corrosive fluid that is always available for free. Used air can be delivered to the ambient with the least precautions and activities. In case of possible leakage, it will cause very few problems.

On the other hand, the implementation of multi-layer heat sinks has not been extensively studied. Wei and Joshi [14] reported that in the water-cooled double-layer microchannel heat sink, for materials with relatively low thermal conductivities relative to other metallic materials, such as steel, adding more layers of microchannels increases the overall thermal resistance. Lei et al. [15] proposed two layers as the optimum number of layers for water-cooled square channel heat sinks. Salimpour and Al-Sammarraie [16] reported that using more than two layers in a water-cooled heat sink is far less effective and hence is not recommended. Bayer et al. [17] studied double-layered wavy microchannel heatsinks enhanced by porous ribs. They used artificial neural networks trained by CFD results to find the effects of waviness on pressure drop and Nusselt number for Reynold number range between 100 and 800. They observed that using a straight channel at the bottom and a wavy channel at the top results in a better thermal efficiency factor.

So, most studies have focused on double-layer heat sinks with water-based coolant medium [18-21]. Against a water-based heat sink in which two layers of mini channels were sufficient, in an air-cooled heat sink, the story is different. As will be shown, an air-cooled multi-layer mini-channel heat sink (MLMC heat sink) has its own superiorities (Fig. 1).

Fig. 1: Multi-layer mini-channel heat sink constructed by authors.

To better understand the benefits of MLMC heat sink, it is required to have a reliable method to predict its thermal performance. To the best authors' knowledge, there is no straightforward method for the thermal performance prediction of the MLMC heat sink. In this study, an innovative analytical method based on straight fin efficiency is implemented. As shown, this method, despite its simplicity, is reliable, even for low thermal conductivity materials such as stainless steel or even materials with lower thermal conductivity.

The method, itself, requires knowing the heat transfer of a simultaneously developing flow in a rectangular duct in which, both the velocity and temperature profiles develop in the entrance region. In many industrial applications, it may be reasonable to ignore the entrance region; however, in the case of a heat sink due to its length, it is almost impossible to ignore the entrance region impact. Indeed, heat sink significantly relies on the high heat transfer coefficient in the entrance region. Unfortunately, little attention has been paid to simultaneously hydrodynamically and thermally developing flow even between paralleled plates [22]. Very limited numerical studies can be found in the literature regarding hydrodynamically developed and thermally developing fluid flows [23-26], and far less literature can be found for simultaneous developing flow. Therefore, in this study, a thorough numerical investigation was performed to simulate and correlate simultaneous developing flow in a rectangular duct.

The structure of this study is as follows: Initially, developing flow for a wide range of Re numbers and channel widths is studied to find proper correlations for both thermal and hydrodynamical developing flow to predict the Nu inside the channel (discussed in Section 2). As in a heat sink, both developing and developed flow may be observed at the same time, these correlations should predict Nu for both types correctly. Section 3 is devoted to developing an analytical method for modelling MLMC heat sink, which is followed by a complementary section for validation of the proposed method (Section 4). Throughout the validation process, the model prediction results are compared against two-dimensional (2-D) and three-dimensional (3-D) numerical simulations of MLMC heat sink. The superiority of an MLMC heat sink is discussed in Section 5 by comparing the entropy generation of an equivalent plate-fin heat sink with MLMC heat sink. Results are summarized in Section 6 and supplementary material is presented in Appendix I.

2. Hydrodynamically and thermally developing flow in a rectangular duct

For a multilayer heat sink, depends on dimensionless parameters (i.e., Re, Pr, and L/W), it is very common to find developing, and developed flow in each individual channel (shown in Fig. 2). The theories of developed flow in rectangular ducts are well established. Even theories of hydrodynamically developed-thermally developing flow have reached a fairly mature level [24-26]. However, simultaneous hydrodynamically and thermally developing flow even between parallel plates is still at the research level [22]. In most industrial applications such as industrial heat exchangers with a relatively long tube, it is reasonable to neglect the entrance length in comparison with the total length; however, in a heat sink, the L/W is not large enough to neglect the entrance length. Moreover, it is more beneficial to utilize the developing flow to optimize heat sink design, since the heat transfer in this region is considerably high [27]. It is noteworthy that for this confined flow, even at early stages where the thickness of the boundary layer is much smaller than the channel width, it is not possible to approximate the heat transfer over each individual wall of the channel with unconfined heat transfer over flat plates. Even the developing flow for the simplest confined case (e.g., a parallel plate) differs from the flow over a flat plate. Indeed, in a confined internal flow, $\mathrm{d}P/\mathrm{d}z$ (pressure gradient along the channel axis, see Fig. 2) is the main driver of flow which cannot be ignored, while over a flat plate, $\mathrm{d}P/\mathrm{d}z = 0$. So, unlike a flat plate,

$\frac{\partial^2 V_z}{\partial z^2}$ at the edge of the boundary layer is not equal to zero [28]. Furthermore, since the flow is confined, the axial velocity (V_z) out of the boundary layer is not constant and $\frac{\partial V_z}{\partial z} \neq 0$. Therefore, the velocity profile in a rectangular channel even at its entrance is basically different from a flat plate. For a constant properties laminar flow, the steady-state three-dimensional governing equations and related boundary conditions in a mini-channel with width W and length L, are given below.

-Continuity equation:

$$\nabla.\vec{V} = 0 \tag{1}$$

-Momentum-conservation equation:

$$\rho(\vec{V}.\nabla\vec{V}) = -\nabla P + \mu(\nabla.\nabla\vec{V}) \tag{2}$$

-Energy-conservation equation:

$$\rho c_P(\vec{V}.\nabla T) = k_{\mathrm{f}}\nabla^2 T \tag{3}$$

The boundary conditions are:

-At the inlet ($z = 0$):

$$\vec{V} = [0,0,U_{\mathrm{in}}], T = T_{\mathrm{in}} = T_\infty \tag{4}$$

- At the outlet ($z = L$):

$$P = P_{\mathrm{out}} = 0 \text{ Pa} \tag{5}$$

At the peripheral walls, constant wall temperature and no-slip condition ($y = W/2$ and $x = 0$):

$$T = T_{\mathrm{w}}, \vec{V} = \vec{0} \tag{6}$$

-Symmetry condition ($y = 0$ and $x = W/2$):

The mini-channel and its boundary conditions are shown in Fig. 2.

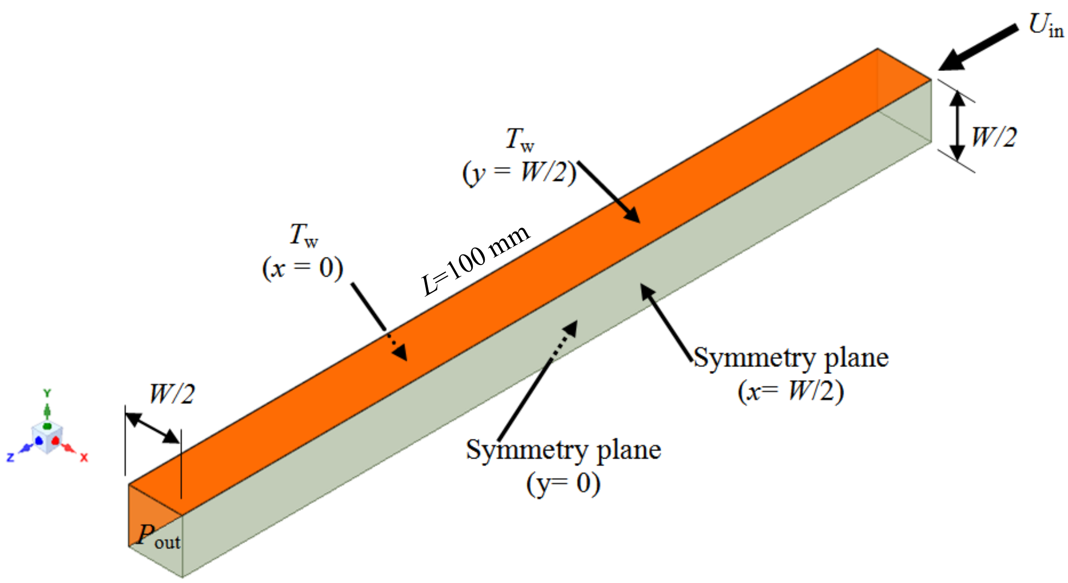

Fig. 2: Mini-channel and boundary conditions.

To solve the above equations numerically a fine, structured grid was prepared. It is vital to have fine grids in the vicinity of the walls and inlet, to enhance the accuracy of results. The numerical studies were accomplished for the following conditions: $W = 2$, 5, 10, and 20 mm, Re = 40, 100, 400, 500, 1500, and 2100 with the channel length of 100 mm and Pr = 0.73. Equations were solved numerically, using Ansys-Fluent 18. Simple algorithm was used for pressure-velocity coupling and second-order upwind method for momentum and energy discretization. Residuals were set to 10^{-6} and 10^{-9} for continuity and energy equations, respectively. Grid independence study was performed and 5×10^6 cells were selected for further investigation for that, the distance of the first girds to the adjacent walls and the inlet was 2×10^{-6} mm. Fig. 3 shows a sample of grid independence study for $Re = 400$.

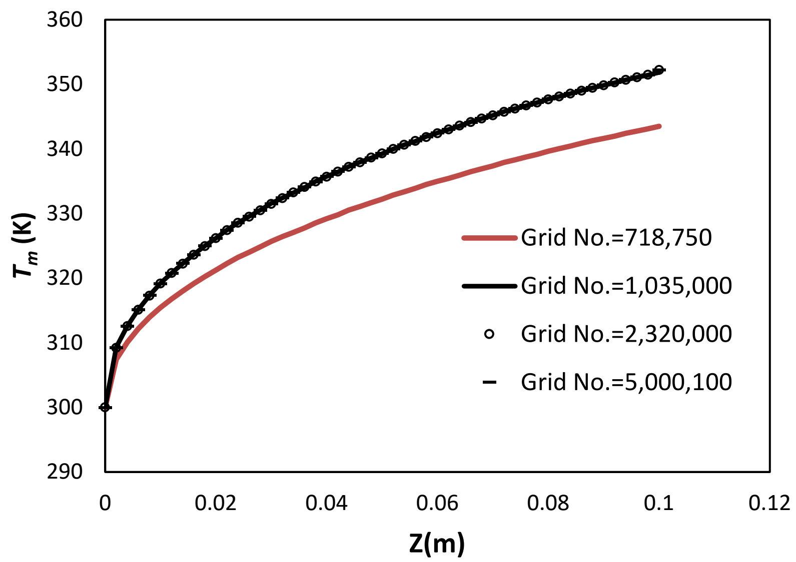

Fig. 3: Profile of T_m along channel length for different grid numbers. Note that the results for grid numbers beyond 1 million almost fall on top of each other.

The convective heat transfer coefficient can be defined in two ways. The first one is $h = q"/(T_{\mathrm{w}} - T_{\mathrm{m}})$ as it is common for internal flow, where T_{m} is defined as:

$$T_{\mathrm{m}} = \frac{\int V_{\mathrm{z}} T.dA}{\int V_{\mathrm{z}}.dA} \qquad (7)$$

However, it is more beneficial to define $h_\infty = q"/(T_{\mathrm{w}} - T_\infty)$, where T_∞ is the intake ambient temperature at the inlet of the channel. As in heat sink applications, the heat flux is high; it is rational to expect different T_{m} at the outlet of each layer (row) of MLMC. However, it is not possible to estimate T_{m} for each layer of MLMC using conventional analytical methods and the problem shall be solved numerically. Indeed, aside from the first layer for which the heat sink bottom temperature value is known (as the boundary condition, for the other layers, the wall temperatures, and consequently heat flux values, are unknown. Hence, the heat transfer between layers is coupled to each other. Therefore, this T_{m} variation in layers will lead to uncertainty in the calculation. Consequently, a novel analytical method is proposed in the upcoming sections to estimate heat transfer in an MLMC heat sink based on h_∞. Both $Nu = \frac{hW}{k_{\mathrm{f}}}$ and $Nu_\infty = \frac{h_\infty W}{k_{\mathrm{f}}}$ are discussed in this article.

It is known that the main variable in developing flow is Z^* [29]:

$$Z^* = \frac{z/W}{Re.Pr} \qquad (8)$$

For all cases, in every 1 mm along the channel length, T_{m} is calculated and Nu versus Z^* are extracted. Later, in each Z^* the calculated Nus are averaged which results are presented in Fig. 4.

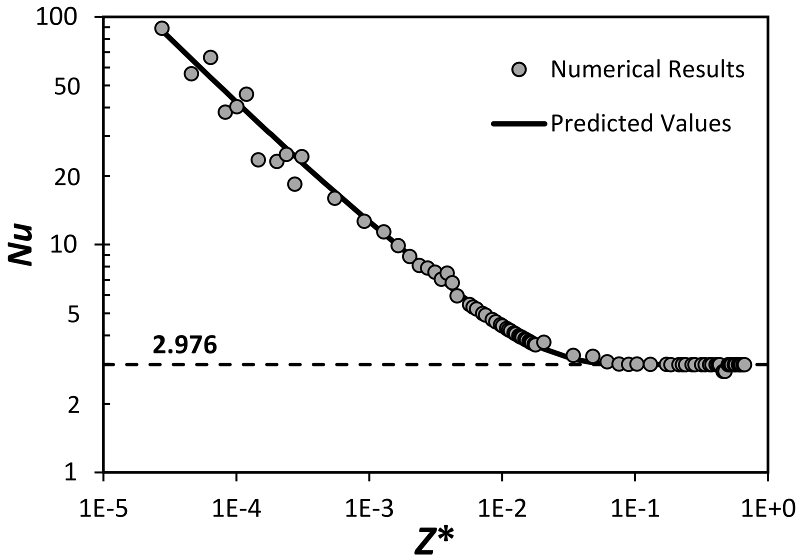

Fig. 4: Variation of Nu against Z^* ($Pr = 0.73$).

As shown in Fig. 4, for $Z^* > 0.1$, Nu_∞ approches 2.98 which is in agreement with the literature results [30]. Fig. 5 shows the variation of temperature patterns for different Z^*. Four different equally spaced sections along a duct are chosen and temperature contours are plotted for each section as demonstrated in Fig. 5. Heat diffuses gradually from the walls to the core of the flow. Since air velocity is very small near corners, a hot zone can be observed in duct corners. So, it is expected that local heat transfer varies considerably from the corner to the midplane of the duct (See Fig. 7). The black solid curved line in each quarter of the figure shows the isothermal line of $T = 320$ K. Furthermore, the shape and location of the isothermal line varies along the duct which is attributed to the development of the thermal boundary layer.

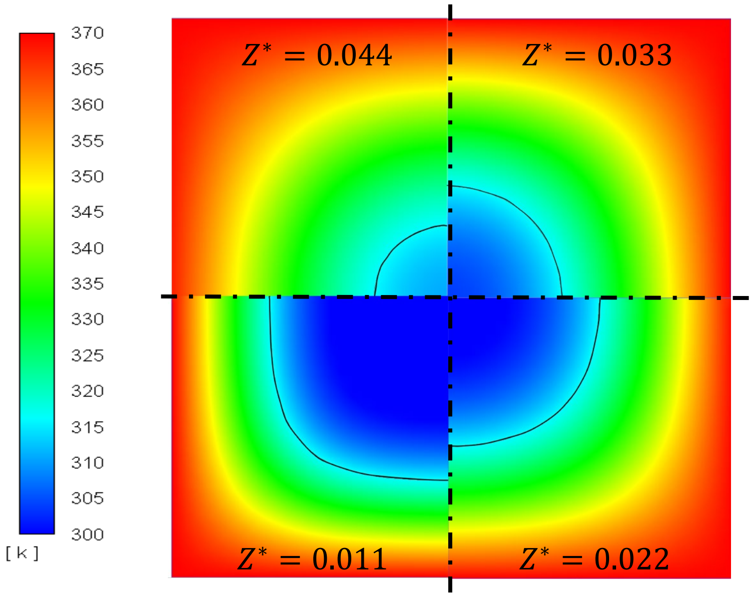

Fig. 5: Variation of temperature contours for different Z^* ($Pr = 0.73$).

Finally, after several tries, the following correlation is proposed (RMSE=4.6):

$$Nu(Z^*) = 0.178\, {Z^*}^{-0.5868} \exp(-59.2\, Z^*) + 2.98 \qquad 10^{-5} < Z^* < 0.7 \tag{9}$$

the average Nu is:

$$\overline{Nu}(Z^*) = \frac{1}{Z^*} \int_0^{Z^*} Nu.\, dZ^* \tag{10}$$

and can be estimated by the following correlation:

$$\overline{Nu}(Z^*) = \left(7.86 + \frac{0.501}{Z^*}\right)^{0.529} \tag{11}$$

The variation of the average Nu against Z^* is shown in Fig. 6.

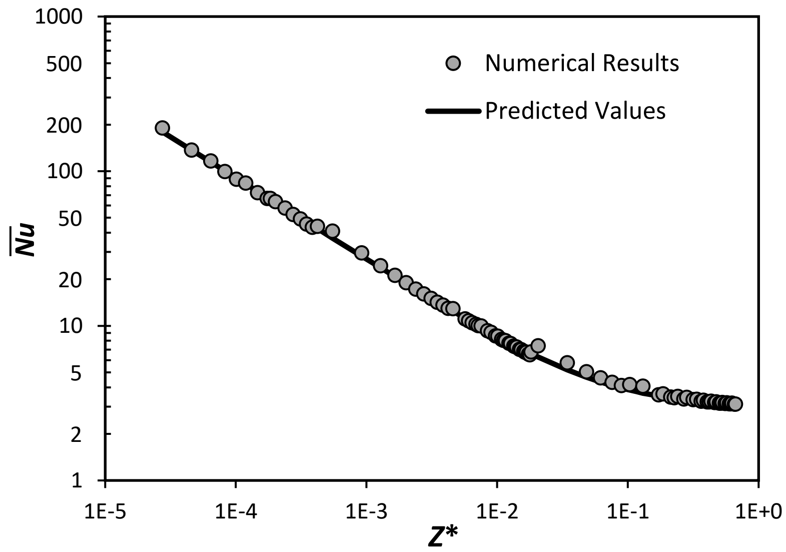

Fig. 6: Variation of $\overline{Nu}$ against Z^* ($Pr = 0.73$).

To find Nu_∞, the value of h_∞ was estimated on every node along the wall. The variation of h_∞ along the wall for the first 0.1 m of the channel is shown in Fig. 7. It can be seen from this figure that h_∞ varies from nearly zero at the corners of the duct to a maximum value of around 25 W/m^{2}K at the centre. It is noteworthy that the aforementioned approach leads to thousands of data that have to be averaged to calculate h_∞.

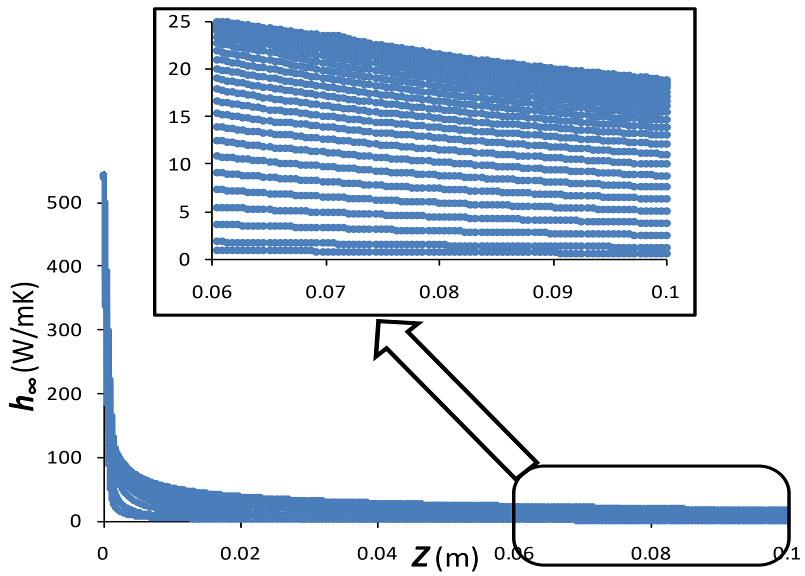

Fig. 7: Variation of h_∞ and the zoom-in view of the graph ($Re = 1500, W = 5$ mm).

The variation of Nu_∞ against Z^* is depicted in Fig. 8. As it is expected, Nu_∞ approaches infinity at small values of Z^*. Since at large values of Z^* fluid-solid wall temperature difference approaches zero, it is expected that Nu_∞ also approaches zero.

We now present a correlation to predict Nu_∞. Since both developing and developed flows can be observed simultaneously in an MLMC heat sink, the correlation must cover both zones.

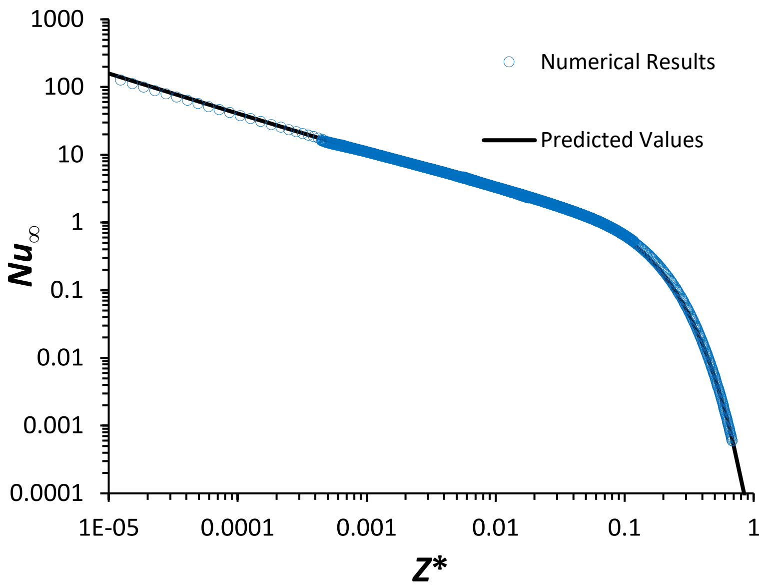

Fig. 8: Variation of Nu_∞ against Z^* ($Pr = 0.73$).

For a developing flow, by scale analysis, it is known that Nu_∞ is [29]:

$$\lim_{Z^* \to 0} Nu_\infty \propto Z^{*-n} \tag{12}$$

where for circular duct, n is something around 0.5. Furthermore, for fully developed flow in a rectangular cross-section, as discussed in Appendix I, Nu_∞ is:

$$\lim_{Z^* \to \infty} Nu_\infty \propto \exp\left(-11.9 Z^*\right) \tag{13}$$

Considering the discussed limiting cases and with trial and error, the following correlation is introduced:

$$Nu_\infty(Z^*) = \left(1.21 + 0.158\, Z^{*-0.6}\right) \exp(-11.3\, Z^*)$$
$$10^{-5} < Z^* \tag{14}$$

for which RMSE is 0.25. In the extreme boundaries, Eq. (14) follows the asymptotic values presented in Eq. (12) and Eq. (13). However, the power of Z^* is -0.6 instead of -0.5.

In the same way, the average Nu_∞ is proposed as:

$$\overline{Nu}_\infty(Z^*) = \left(0.4 \exp(-3.2\, Z^*) + \frac{0.566}{Z^{*0.251}}\right)^{2.52}$$
$$10^{-5} < Z^* \tag{15}$$

in which:

$$\overline{Nu}_\infty(Z^*) = \frac{1}{Z^*} \int_0^{Z^*} Nu_\infty . dZ^* \tag{16}$$

The variation of the average $\overline{Nu}_\infty$ with Z^* is shown in Fig. 9, which shows a comparison of predicted values (from Eq. (15)) against numerical results from the present model.

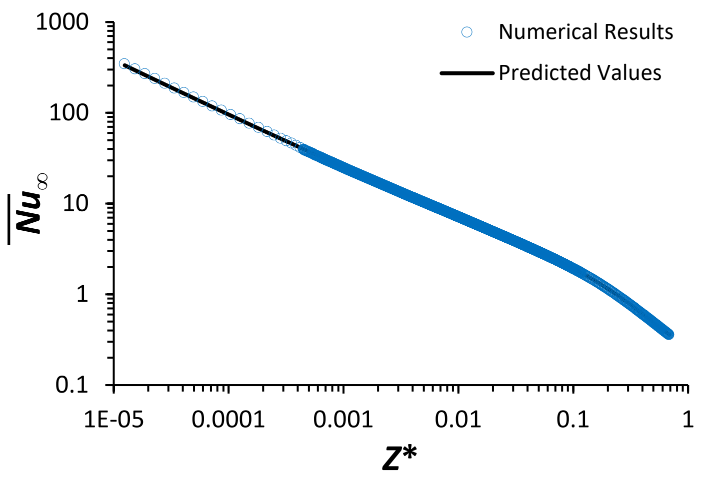

Fig. 9: Variation of Nu_∞ against Z^* ($Pr = 0.73$).

To validate the proposed approach, the same procedure was considered for a duct with a circular cross-section and compared against literature results including Churchill and Ozoe's correlation [31] for simultaneous developing flow inside a circular duct (Eq. (17)) and the available data [32-34] tabulated in Ref. [35].

$$Nu_{\text{circular}}(Z^*) = \frac{0.637[(4/\pi)Z^*]^{-1/2}}{[1 + (Pr/0.0468)^{2/3}]^{1/4}} \tag{17}$$

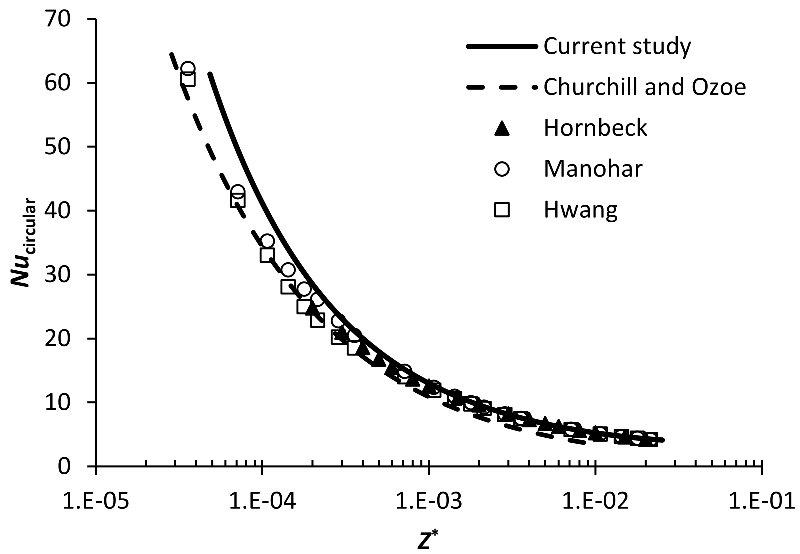

Fig. 10: Variation of Nu_{circular} against Z^* ($Pr = 0.73$) for circular duct.

3. Analytical approximation of MLMC heat sink performance

Figure 11 shows a sketch of a typical MLMC heat sink which is composed of several layers of mini-channels. In this figure, t_{v} and t_{h} are vertical wall and horizontal wall thickness, respectively and commonly limited by construction constraints.

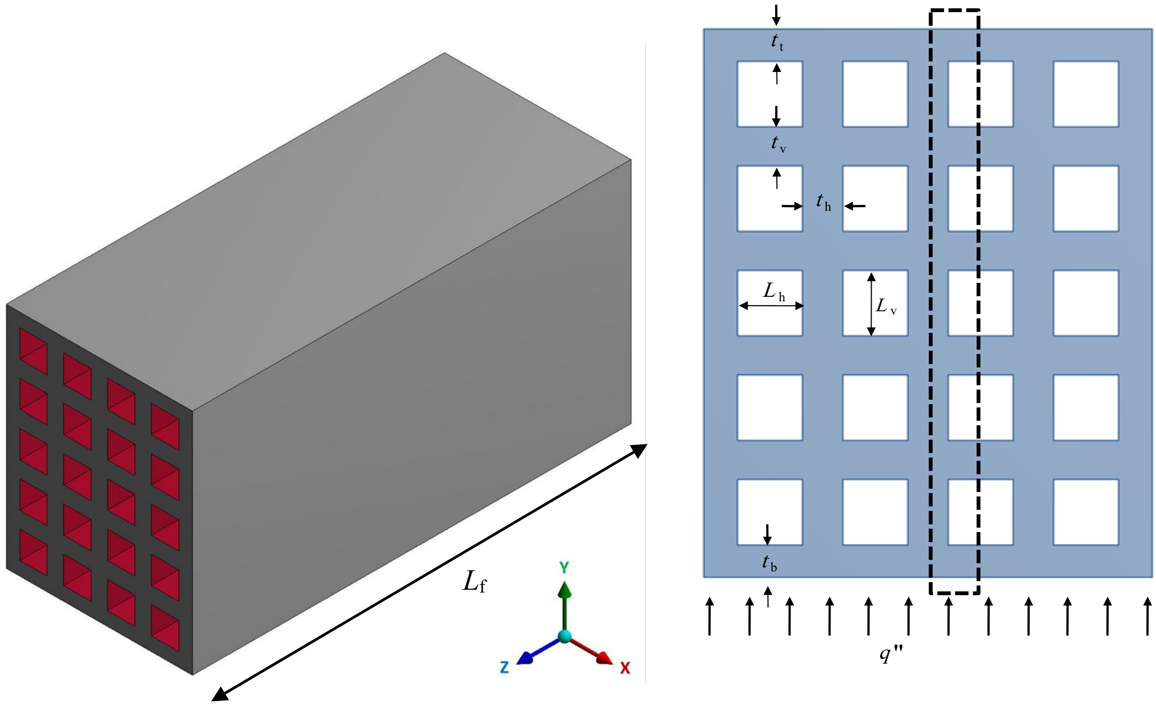

Fig. 11: 3-D sketch and front view of a typical MLMC heat sink including contributing geometrical parameters.

For small values of wall thickness, the wall may be torn out during cutting or drilling. The thickness of the heat sink bottom plate and top plate are indicated by t_b and t_t, respectively. Those thicknesses may be greater or equal to t_h. In the following section, an MLMC will be analysed based on straight fin theory.

3.1 Straight fin theory

Figure 12 shows a schematic view of a straight fin subjected to convection heat transfer with ambient temperature, T_∞ and average convection coefficient of $\bar{h}$. The fin base is at the temperature T_b or temperature difference $\theta_\mathrm{b} = T_\mathrm{b} - T_\infty$.

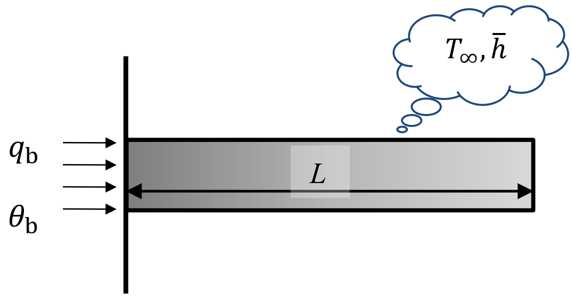

Fig. 12: A schematic view of a straight fin.

For a straight fin shown in Fig. 12, the total heat flows to the base of the fin (q_b) is [36]:

$$q_\mathrm{b} = \sqrt{\bar{h} P k_\mathrm{s} A}\theta_\mathrm{b} \tanh(mL) \tag{18}$$

where $\bar{h}$ is the average heat transfer coefficient, A is the fin cross-section area, k_s is the solid thermal conductivity, P is the perimeter of the fin and L is the fin length.

$$m = \sqrt{\bar{h}P/k_s A} \tag{19}$$

An equivalent convective coefficient can be introduced in a way that:

$$q_b = h_{eq} A \theta_b \tag{20}$$

So:

$$h_{eq} = \sqrt{\frac{\bar{h}Pk_s}{A}} \tanh\left(\sqrt{\bar{h}P/k_s A}\, L\right) \tag{21}$$

This equivalent convection coefficient is the base of this study.

3.2 Sub-areas in an MLMC

To establish a 2-D analytical method, due to its symmetrical structure, only one-half of the channels in MLMC are considered for the study. The separated areas are shown in Fig. 13. Based on this figure, the area is divided into four sub-areas. The main part is considered a straight fin and is called the "Primary Fin" (coloured blue in Fig. 13). All parameters related to this area will be indicated by subscript "I". The branching areas are also considered as straight fins named "Secondary Fin" (coloured red in Fig. 13) and will be specified by subscript "II". The remaining areas are the "Base Area" (coloured brown in Fig. 13) and an insulated zone, i.e., "Top Area" (coloured yellow in Fig. 13). In the following, each sub-area is considered in detail.

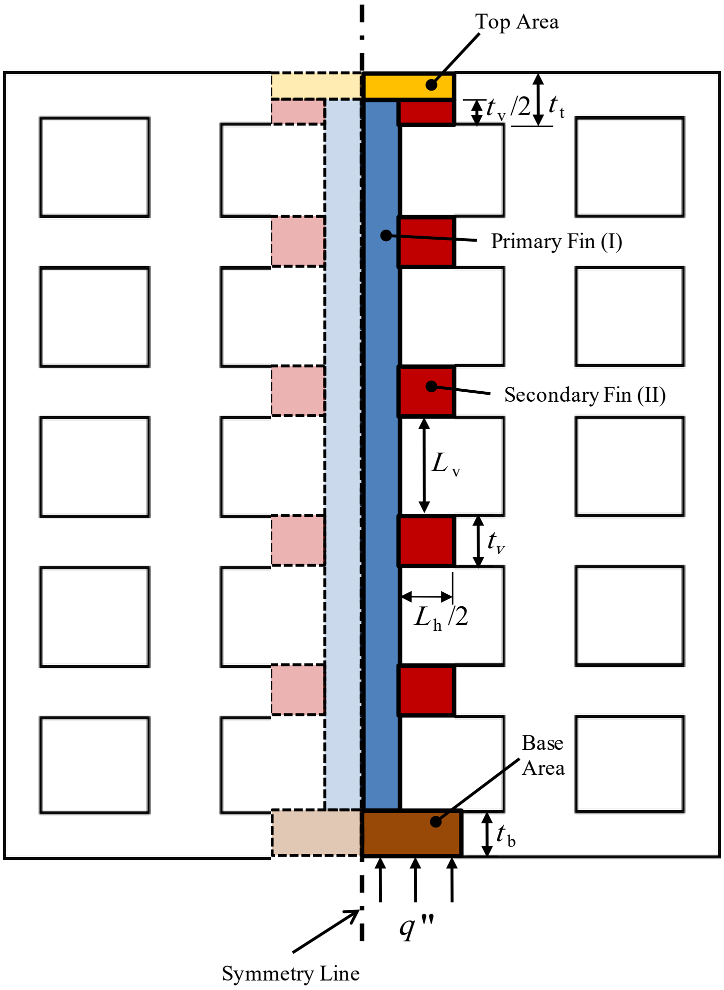

Fig. 13: Separated areas of heat sink for study.

3.3 Secondary fin

Figure 14 shows a schematic view of "Secondary Fin". The base of the fin is at the temperature T_{II} and $\theta_{\mathrm{II}} = T_{\mathrm{II}} - T_\infty$. T_∞ is the ambient temperature. It is noteworthy that θ_{II} is different for each row and will be calculated later.

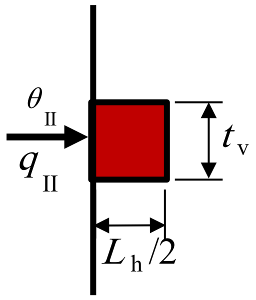

Fig. 14: Secondary Fin schematic.

In the same way, for the secondary fin, the equivalent convective coefficient is:

$$h_{\mathrm{eq}} = \sqrt{\frac{2\bar{h}k_{\mathrm{s}}}{t_{\mathrm{v}}}}\tanh\left(\underbrace{\sqrt{2\bar{h}/k_{\mathrm{s}}t_{\mathrm{v}}}}_{m_{\mathrm{II}}}\frac{L_{\mathrm{h}}}{2}\right) \tag{22}$$

The heat dissipation from the Primary Fin is partly convective and partly conductive. However, by introducing the equivalent convective coefficient, it can be assumed that convection is the only mode of heat transfer over the Primary Fin. In the next part, the temperature variation along the Primary Fin and consequently θ_s will be calculated.

3.4 Primary fin and top area

The longitudinal wall can be considered again as a straight fin subjected to channel convective heat transfer ($\bar{h}$) and equivalent convective heat transfer (h_{eq}), intermittently (Fig. 15).

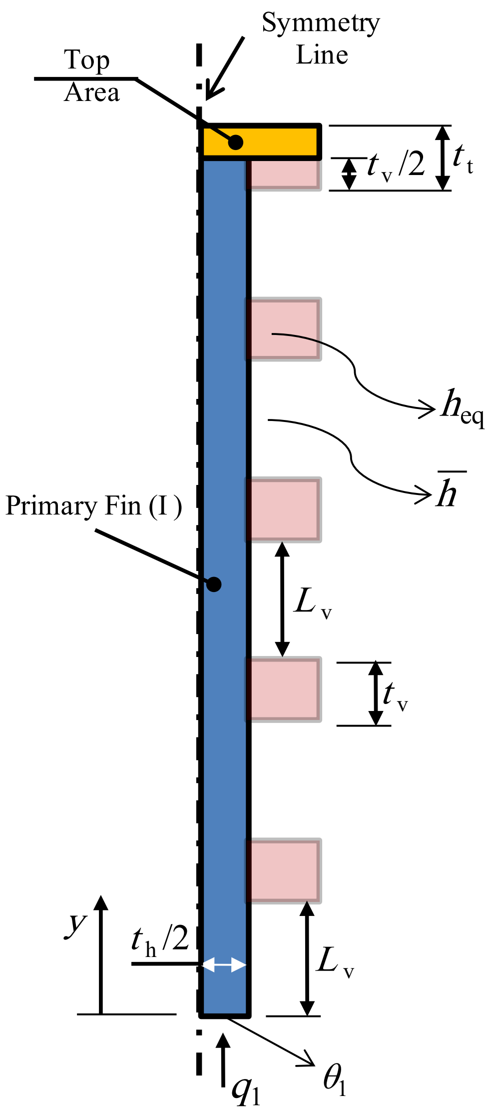

Fig. 15: Simplified version of the Primary Fin.

To simplify the problem, assuming a uniform heat transfer coefficient (called effective heat transfer coefficient) which is the area-weighted average of those two heat transfer coefficients:

$$h_{eff} = \frac{N.L_v.\bar{h} + (N - 0.5).t_v.h_{eq}}{\underbrace{N.L_v + (N - 0.5).t_v}_{L_{eff}}} \tag{23}$$

The extra length over $t_v/2$ does not participate significantly in heat transfer. Therefore, this zone is assumed insulated and with zero temperature gradient. The total amount of heat that flows into the “Primary Fin” and dissipated into the air is q_1 at the temperature difference of θ_1 (different from MLMC heat sink base temperature difference θ_s).

Rewriting Eq. (18) for the Primary Fin:

$$q_1 = \underbrace{\sqrt{2h_{\mathrm{eff}}k_s t_h}\tanh(m_I L_{\mathrm{eff}})}_{E}\,\theta_1 \tag{24}$$

L_{eff} is the denominator of Eq. (23) and according to Eq. (19) m_I is:

$$m_I = \sqrt{2h_{\mathrm{eff}}/k_s t_h} \tag{25}$$

The temperature variation along the “Primary Fin” length is [36]:

$$\theta_I = \theta_1 \cosh\big(m_I(L_{\mathrm{eff}} - y)\big) \,/\, \cosh(m_I L_{\mathrm{eff}}),\ 0 \le y \le L_{\mathrm{eff}} \tag{26}$$

where $\theta_I = T_I - T_\infty$. The remaining parameters, i.e., θ_1 and consequently q_1 is calculated in the next section.

3.5 Base area

The “Base Area” is basically different from the horizontal branches (“Secondary Fin”), since it is directly subjected to the heat flux q''.

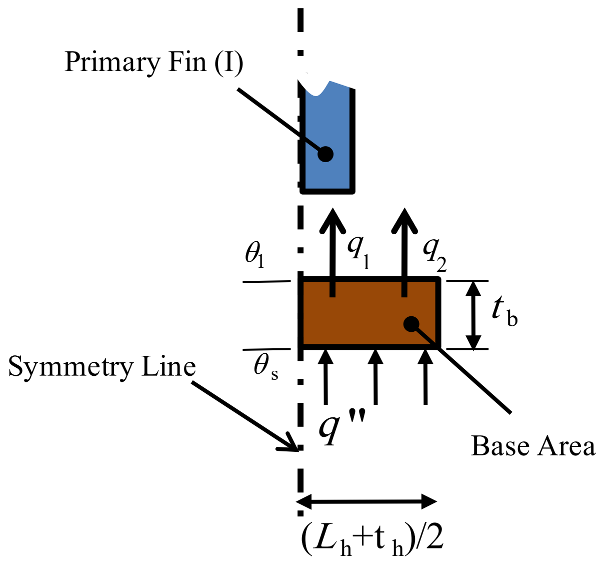

Fig. 16: Heat transfer scheme in the “Base Area”.

As shown in Fig. 16, there are two parallel zones in the “Base Area”. One is beneath the “Primary Fin” and transfers q_1 to it and the other is in direct contact with the air and dissipates q_2. So, by considering Eq. (24):

$$q''.(L_h + t_h) = q_1 + q_2 = E.\theta_1 + \bar{h}.L_h\theta_1 \rightarrow \theta_1 = \frac{q''(L_h + t_h)}{E + \bar{h}.L_h} \tag{27}$$

and finally:

$$q" = k_{\mathrm{s}} \frac{(\theta_{\mathrm{s}} - \theta_1)}{t_{\mathrm{v}}} \rightarrow \theta_{\mathrm{s}} = \theta_1 + \frac{q" t_{\mathrm{v}}}{k_{\mathrm{s}}} \tag{28}$$

4. Validation

Two steps are considered to validate the results. Firstly, it is assumed that the heat transfer coefficient is uniform and constant all over the channel area. A 2-D numerical simulation is performed and the results of the described analytical method are validated against this numerical solution for both high- and low-conductive heat sink materials. Later, a complete 3-D model including both fluid and solid zone is simulated to find out the effect of simplifications used in the described analytical method.

4.1 2-D numerical simulations

The summary of simulated geometry is introduced in Table 1. This geometry was solved numerically and the temperature contour for stainless steel (S.S.) material ($k_{\mathrm{s}} = 13$ W/m.K) is shown in Fig. 17.

Table 1: Geometrical parameters used for the 2-D model.

$t_{\mathrm{v}} = 1.5$ [mm]	$L_{\mathrm{v}} = 3$ [mm]	$L_{\mathrm{h}} = 3$ [mm]
$t_{\mathrm{t}} = 1.5$ [mm]	$t_{\mathrm{b}} = 1.5$ [mm]	$t_{\mathrm{h}} = 1.5$ [mm]
$\bar{h} = 26.8$ [W/m^{2}K]	$N = 5$ [-]	$q" = 8$ kW/m^2

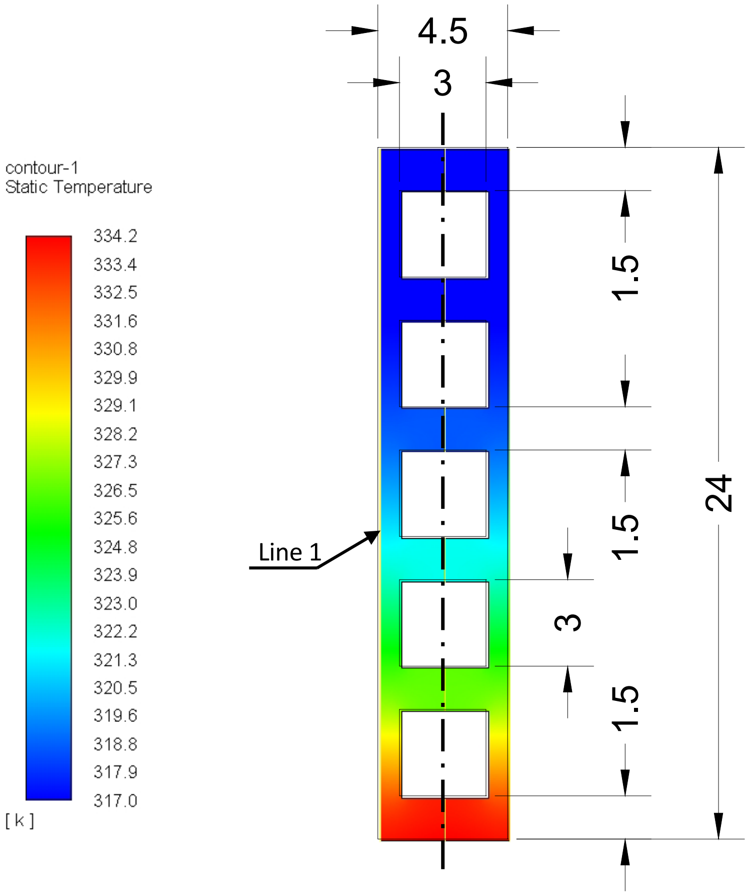

Fig. 17: Temperature contours for the 2-D geometry for k_s = 13 W/m.K (S.S. material, all dimensions are in mm).

The geometry was also analysed using the presented analytical solution. The intermediate results are presented in Table 2 for more clarity for both S.S. as a low thermal conductivity material and aluminium (Al.) as a high thermal conductivity material.

Table 2: Output parameters.

High conductivity (Al.) (k_s = 200 [W/m.K])	Low conductivity (S.S.) (k_s = 13 [W/m.K])	Equation
h_{eq} = 55.5 [W/m^{2}K]	h_{eq} = 55.4 [W/m^{2}K]	Eq. (22)
m_{II} = 13.6	m_{II} = 53.4	Eq. (22)
L_{eff} = 21.8 [mm]	L_{eff} = 21.8 [mm]	Eq. (23)
h_{eff} = 36.3 [W/m^{2}K]	h_{eff} = 35.1 [W/m^{2}K]	Eq. (23)
E = 1.52 [W/K]	E = 1.03 [W/K]	Eq. (24)
m_I = 15.6	m_I = 61.0	Eq. (25)
θ_1 = 22.4 [K]	θ_1 = 32.2 [K]	Eq. (27)
θ_s = 22.5 [K]	θ_s = 33.2 [K]	Eq. (28)

Figure 18 shows the variation of temperature along the fin height (Line 1 in Fig. 17) for both thermal conductivities (Al. and S.S.) which were calculated based on the proposed analytical solution and compared against the numerical results. An excellent agreement can be observed for both thermal conductivities which shows the ability of the proposed method in heat transfer prediction for a broad range of materials.

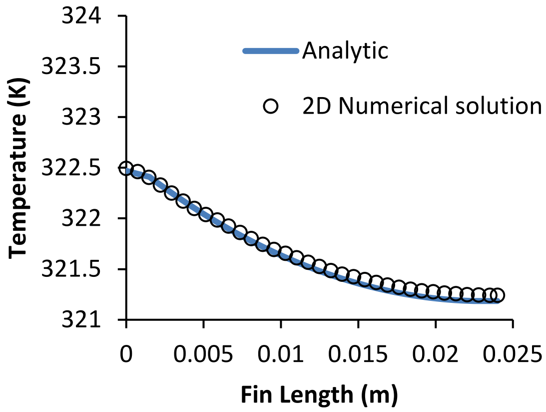

a) Al. heat sink

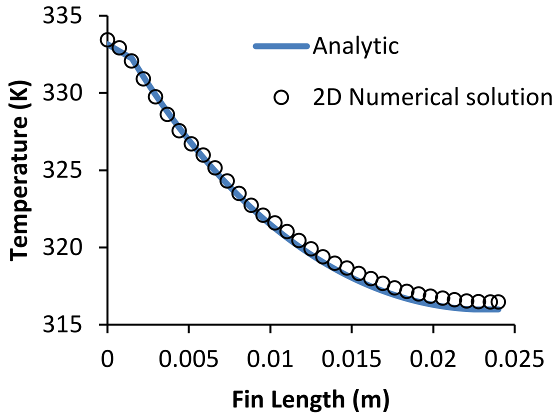

b) S.S. heat sink

Fig. 18: Comparison of temperature variation along heat sink height based on analytical method and the 2-D numerical solution.

4.2 3-D numerical simulations

The next step is devoted to comparing the 2-D approximation with a 3-D solution under real operating condition. In this regard, a 3-D model of the mentioned geometry introduced in Table 1, was prepared with the heat sink length of $L_{\mathrm{f}} = 0.05$ m. For the air average velocity of 2.95 m/s in each channel, Re = 480 and Pr = 0.73. Using Eq. (15) for $L_{\mathrm{f}} = 0.05\,\mathrm{m}$, $\overline{Nu}_{\infty} = 3.06$ and consequently, $\bar{h} = 26.8$ [W/m^{2}K] which is equal to the value introduced in Table 1. Equations were numerically solved via the described method. The variation of temperature along the heat sink length can be observed in Fig. 19. As is expected, the hottest zone can be observed at the end of the heat sink.

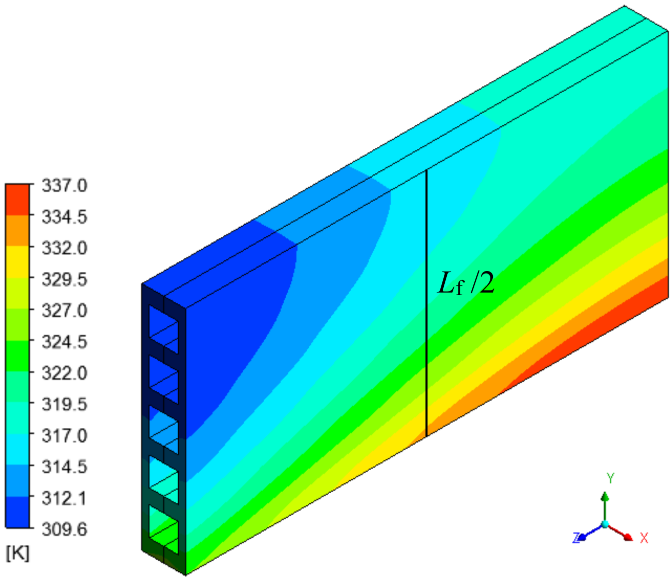

Fig. 19: Heat sink temperature contour.

In that regard, in Fig. 20 the analytical solution is compared against the results of the 3-D numerical solution, over the line $\frac{L_f}{2}$ which display a very good agreement between results.

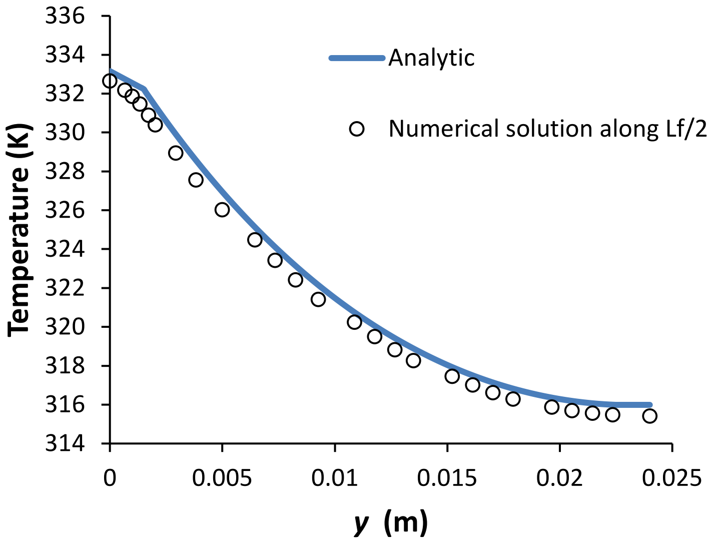

Fig. 20: Comparison of temperature variation along $\frac{L_f}{2}$ line calculated by both analytical and numerical solutions.

5. Further discussion

To show the superiority of an MLMC heat sink, this heat sink was compared with an equivalent plate-fin heat sink. A plate-fin heat sink as a conventional type of heat sink is widely used in electronic applications (e.g., CPU cooling). Figure 21 shows the simulated plate heat sink inside an adiabatic duct.

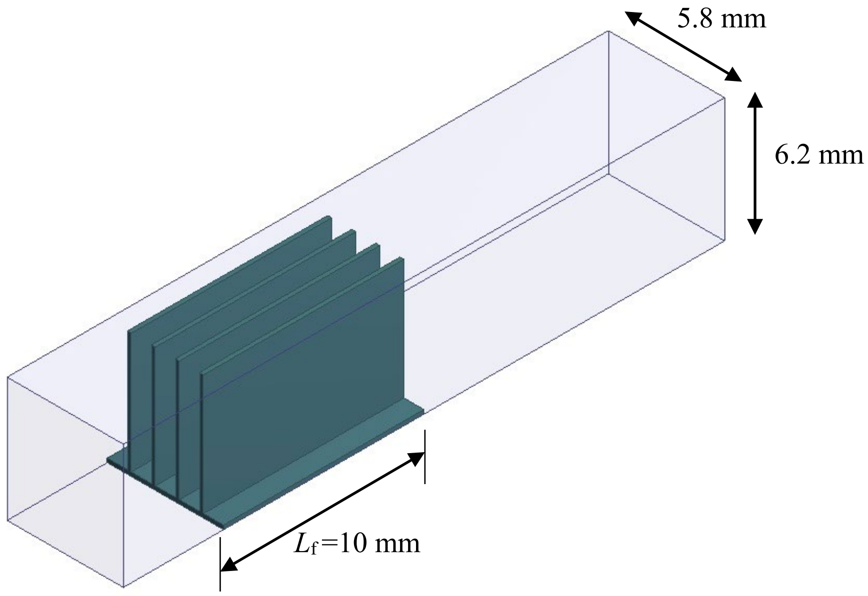

Fig. 21: Simulated plate-fin heat sink.

The schematic front views of both heat sinks (MLMC and straight fin) are presented in Fig. 22. The heat sink length is $L_\mathrm{f} = 0.01$ m and the heat sink base is subjected to a uniform heat flux $q" = 8$ kW/m^2. The inlet air velocity is 3 m/s and therefore, the air mass flow rate was $m^{\cdot} = 1.14 \times 10^{-4} \frac{\mathrm{kg}}{\mathrm{s}}$. Both heat sinks are made of aluminium.

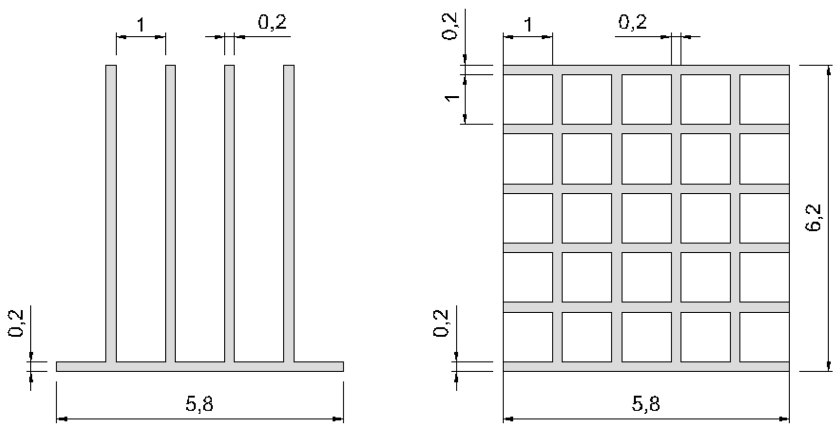

Fig. 22: Heat sinks geometrical parameters (all dimensions are in mm).

Both cases were simulated numerically by the described method. Grid independence study was conducted on cases; however, for sake of brevity is not presented here. Temperature contours of both fins are presented in Fig. 23. This figure shows clearly that the MLMC heat sink operates at a temperature much lower than the plate-fin heat sink. The average base temperature of MLMC is 307 K while it is 310 K for the plate-fin heat sink.

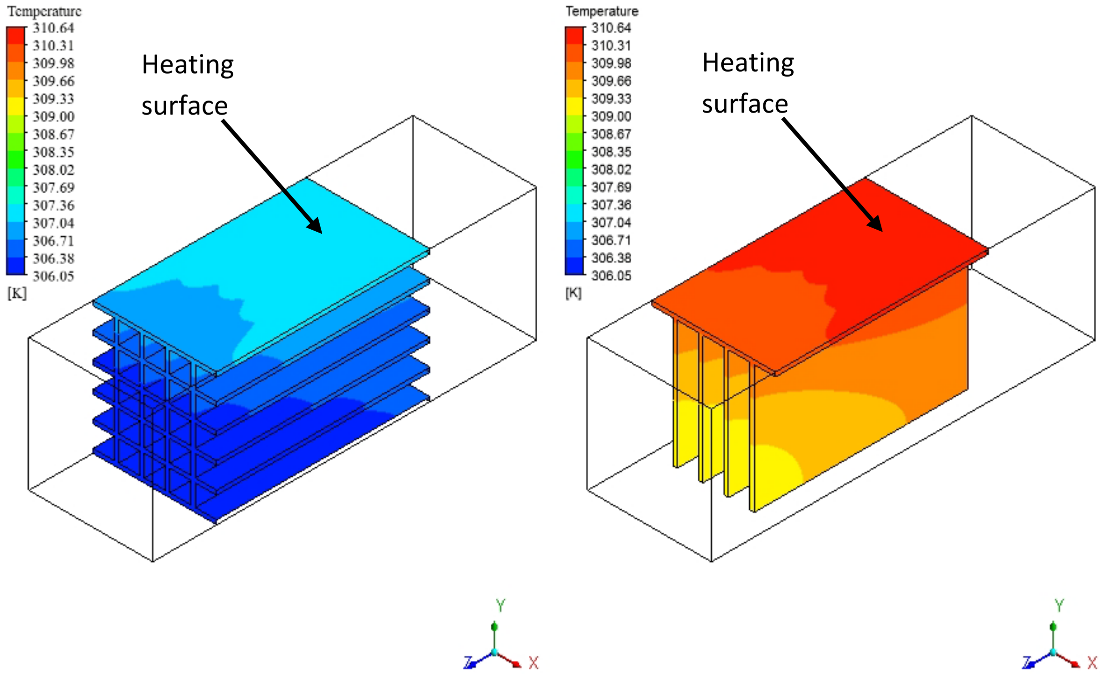

Fig. 23: Comparison of working temperatures of MLMC heat sink (left side) and plate-fin heat sink (right side).

The temperature contours at fin outlets are also compared in Fig. 24. Although the average outlet temperature for both heat sinks is the same (because of the constant heat flux boundary condition), the temperature contour in MLMC is much more uniform which shows that heat is distributed uniformly throughout the heat sink. In contrast, two wide hot zone and cold zone can be observed in the temperature contour of the plate-fin heat sink which specifies the dead zone in which heat transfer is poor.

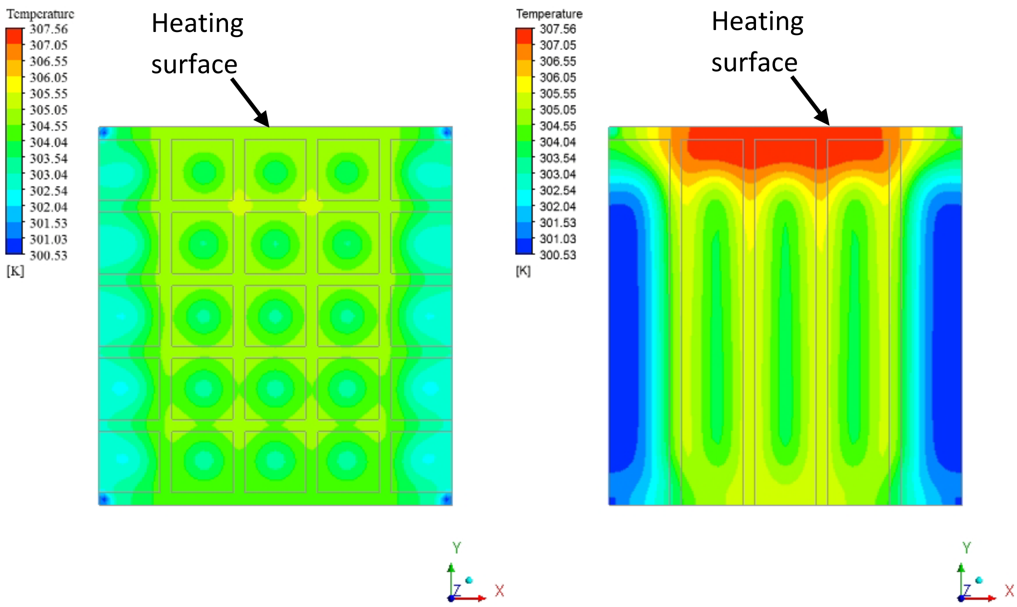

Fig. 24: Comparison of outlet temperatures of MLMC heat sink (left side) and plate-fin heat sink (right side).

However, the pressure drop across the MLMC heat sink is higher than the plate-fin heat sink. The pressure drop for the current MLMC and plate-fin heat sinks is 36 Pa and 15 Pa, respectively. The pressure drop across the heat sink is normally compensated by a DC fan and usually is not a serious matter.

Performance factor (PF) is an effective index to compare performance of different heat transfer equipment. It is defined as the ratio of the total heat transfer coefficient for a constant pumping power and temperature difference [37].

$$\mathrm{PF} = \frac{U_{\mathrm{MLMC}}/U_{\mathrm{pf}}}{\left(f_{\mathrm{MLMC}}/f_{\mathrm{pf}}\right)^{1/3}} \tag{29}$$

The total heat transfer coefficient is defined as:

$$U = \frac{q}{T_{\mathrm{s}} - T_{\mathrm{f}}} \tag{30}$$

where q is the total heat flux to the heat sink and T_{s} and T_{f} are average heat sink base temperature and average air temperature. The average fluid temperature is approximated as $T_{\mathrm{f}} = \frac{T_{\mathrm{in}}+T_{\mathrm{out}}}{2}$ where T_{in} and T_{out} are inlet and outlet temperatures, respectively.

The friction factor is defined as:

$$f = \frac{\Delta P}{\frac{1}{2}\rho \bar{U}^2}\frac{D_{\mathrm{h}}}{L_{\mathrm{f}}} \tag{31}$$

where, ΔP is the pressure drop across the heat sink, $\bar{U}$ is the air average velocity, $\rho = 1.0585$ kg/m3 is the air density and D_{h} is the heat sink hydraulic diameter which is defined as four times of channel cross-section area (A_{c}) to the wetted perimeter ($\mathcal{P}$). Required parameters are listed in Table 3 and Table 4.

Table 3: Input parameters of Eq. (30) and Eq. (33).

Parameter	MLMC heat sink	Plate-fin heat sink	Explanation
U [W/K]	0.0928	0.058	$\frac{q}{T_{\mathrm{s}} - T_{\mathrm{f}}}$
A_{c} [m^2]	2.5×10^{-5}	3×10^{-5}	MLMC: No. of channels (25) times the area of each square (0.001×0.001) Plate fin: No. of passages (5) times the area of each passage (0.006×0.001)
$\mathcal{P}$ [m]	0.1	0.07	MLMC: No. of channels (25) times the perimeter of each square (0.001×4) Plate fin: No. of passages (5) times the area of each passage ((0.006+0.001)×2)
D_{h} [m]	1×10^{-3}	1.714×10^{-3}	$4A_{\mathrm{c}}/\mathcal{P}$
$\bar{U}$ [m/s]	4.31	3.59	$m^{\cdot}/A_{\mathrm{c}}$
f	0.367	0.377	

By plugging in listed input data in Table 3 in Eq. 29, calculated PF will be 1.62. It means that for equal pumping power and temperature difference, the heat transfer in the MLMC heat sink is considerably higher than the plate-fin heat sink.

Another method to assess performance of heat exchanger from heat transfer and pressure drop perspectives is entropy generation [1, 38-40]. Considering the heat sink as a thermodynamic system, the total entropy change across the heat sink is [41]:

$$\Delta s = c_P \ln\left(\frac{T_{\mathrm{out}}}{T_{\mathrm{in}}}\right) - R \ln\left(\frac{1}{1 + \Delta P / P_{\mathrm{amb}}}\right) \quad (32)$$

P_{amb} is the ambient pressure. Eventually, the specific entropy generation is:

$$s_{\mathrm{gen}} = \Delta s - \frac{q/\dot{m}}{T_{\mathrm{s}}} \quad (33)$$

The input parameters of Eq. (32) and Eq. (33) are summarized in Table 4.

Table 4: Input parameters of Eq. (32) and Eq. (33).

$\dot{m}$	1.14×10^{-4}	[kg/s]
c_P	1.016	[kJ/kg.K]
R	0.287	[kJ/kg.K]
q	0.464	[W]
T_{in}	300	[K]
T_{out}	304	[K]
T_{f}	302	[k]
P_{amb}	101	[kPa]

The specific entropy generation for MLMC heat sink was 0.30 J/kg.K and for the plate-fin heat sink was 0.38 J/kg.K which is 27% more than MLMC heat sink. This shows the superiority of the MLMC heat sink.

6. Conclusion

In this study, a new type of air-cooled multi-layer multi-channel (MLMC) heat sink was proposed. To predict the heat transfer rate in the proposed heat sink, the heat transfer in a rectangular channel for simultaneously developing flow was considered. Based on numerical simulations, correlations were proposed to cover both developing and developed airflow in the duct. An innovative analytical solution was proposed to calculate the base average temperature. The method was later compared with the numerical solution of MLMC in both 2-D and 3-D geometries. It was shown that the results of the proposed analytical solution are compatible with 2-D and 3-D numerical solutions, even for materials with relatively low thermal conductivity. Eventually, the MLMC was compared with a plate-fin heat sink, as a conventional type of heat sink widely used to cool electronic devices. For the similar working condition, it was found that MLMC heat sink temperature is much lower than the plate-fin heat sink. Moreover, entropy generation in the plate-fin heat sink was 27% more than MLMC heat sink. Entropy generation is a promising index for showing the superiority of MLMC heat sinks.

Acknowledgements

The research was funded by the UK Engineering and Physical Sciences Research Council (EPSRC) [grant numbers EP/V042149/1, and EP/T03338X/1], and the Ministry of Science and Higher Education of the Russian Federation (Megagrant Project No. 075-15-2019-1888). The authors gratefully acknowledge this support. Data supporting this publication can be obtained on request from cep-lab@imperial.ac.uk.

The authors are also grateful to Mr. Mehdi Karimi, the project manager for providing valuable information and the construction of a prototype.

References

[1] H. Nemati, A general equation based on entropy generation minimization to optimize plate fin heat sink, Eng. J., 22(1) (2018) 159-174.
[2] H. Nemati, M.M. Ardekani, Heat sink evolutionary optimization by natural construction method, Numer. Heat Transf.; A: Appl., 80(4) (2021) 168-183.
[3] L. Lombaard, M. Moghimi, P. Valluri, J. Meyer, Interaction between multiple bubbles in microchannel flow boiling and the effects on heat transfer, Int. Commun. Heat Mass Transf., 129 (2021) 105703.
[4] Y. Lin, Y. Luo, W. Li, Y. Cao, Z. Tao, T.I.-P. Shih, Single-phase and Two-phase Flow and Heat Transfer in Microchannel Heat Sink with Various Manifold Arrangements, Int. J. Heat Mass Transf., 171 (2021) 121118.
[5] A.S. El-dean, O. Hassan, H. Shafey, Heat transfer characteristics of two-phase flow in a double-layer microchannel heat sink, Int. Commun. Heat Mass Transf., 132 (2022) 105899.
[6] S.T. Kadam, R. Kumar, Twenty first century cooling solution: Microchannel heat sinks, Int. J. Therm. Sci., 85 (2014) 73-92.
[7] R. Zhang, M. Hodes, N. Lower, R. Wilcoxon, Water-based microchannel and galinstan-based minichannel cooling beyond 1 kW/cm^2 heat flux, IEEE Transactions on Components, Packaging and Manufacturing Technology, 5(6) (2015) 762-770.
[8] Y. Li, G. Xia, D. Ma, Y. Jia, J. Wang, Characteristics of laminar flow and heat transfer in microchannel heat sink with triangular cavities and rectangular ribs, Int. J. Heat Mass. Tran., 98 (2016) 17-28.
[9] I.A. Ghani, N. Kamaruzaman, N.A.C. Sidik, Heat transfer augmentation in a microchannel heat sink with sinusoidal cavities and rectangular ribs, Int. J. Heat Mass. Tran., 108 (2017) 1969-1981.
[10] P. Gao, S. Le Person, M. Favre-Marinet, Scale effects on hydrodynamics and heat transfer in two-dimensional mini and microchannels, Int. J. Therm. Sci., 41(11) (2002) 1017-1027.
[11] S. Reynaud, F. Debray, J.-P. Franc, T. Maitre, Hydrodynamics and heat transfer in two-dimensional minichannels, Int. J. Heat Mass. Tran., 48(15) (2005) 3197-3211.
[12] H. Nemati, M. Moghimi, J. Meyer, Shape optimisation of wavy mini-channel heat sink, Int. Commun. Heat Mass Transf., 122 (2021) 105172.
[13] A.A. Al-Rashed, A. Shahsavar, O. Rasooli, M. Moghimi, A. Karimipour, M.D. Tran, Numerical assessment into the hydrothermal and entropy generation characteristics of biological water-silver

nano-fluid in a wavy walled microchannel heat sink, Int. Commun. Heat Mass Transf., 104 (2019) 118-126.
[14] X. Wei, Y. Joshi, Stacked microchannel heat sinks for liquid cooling of microelectronic components, J. Electron. Packag., 126(1) (2004) 60-66.
[15] N. Lei, A. Ortega, R. Vaidyanathan, Modeling and optimization of multilayer minichannel heat sinks in single-phase flow, in: International Electronic Packaging Technical Conference and Exhibition, 2007, pp. 29-43.
[16] M.R. Salimpour, A.T. Al-Sammarraie, A. Forouzandeh, M. Farzaneh, Constructal design of circular multilayer microchannel heat sinks, J. Therm. Sci. Eng. Appl., 11(1) (2019).
[17] Ö. Bayer, S.B. Oskouei, S. Aradag, Investigation of double-layered wavy microchannel heatsinks utilizing porous ribs with artificial neural networks, Int. Commun. Heat Mass Transf., 134 (2022) 105984.
[18] W. He, R. Mashayekhi, D. Toghraie, O.A. Akbari, Z. Li, I. Tlili, Hydrothermal performance of nanofluid flow in a sinusoidal double layer microchannel in order to geometric optimization, Int. Commun. Heat Mass Transf., 117 (2020) 104700.
[19] N. Patel, H.B. Mehta, Experimental investigations on a variable channel width double layered minichannel heat sink, Int. J. Heat Mass Transf., 165 (2021) 120633.
[20] L. Liu, Z. Cao, C. Xu, L. Zhang, T. Sun, Investigation of fluid flow and heat transfer characteristics in a microchannel heat sink with double-layered staggered cavities, Int. J. Heat Mass Transf., 187 (2022) 122535.
[21] H. Shen, G. Xie, C.-C. Wang, H. Liu, Experimental and numerical examinations of thermofluids characteristics of double-layer microchannel heat sinks with deflectors, Int. J. Heat Mass Transf., 182 (2022) 121961.
[22] M. Everts, J.P. Meyer, Laminar hydrodynamic and thermal entrance lengths for simultaneously hydrodynamically and thermally developing forced and mixed convective flows in horizontal tubes, Exp. Therm. Fluid Sci., 118 (2020) 110153.
[23] T. Bennett, Refinement of the generalized Graetz problem correlation with new benchmark calculations, J. Heat Transfer, 142(5) (2020) 051802.
[24] T. Bennett, Correlating laminar convection in slots with developing flow, Int. J. Heat Mass Transf., 162 (2020) 120346.
[25] L. Su, Z. Duan, B. He, H. Ma, X. Ning, G. Ding, Y. Cao, Heat transfer characteristics of thermally developing flow in rectangular microchannels with constant wall temperature, Int. J. Therm. Sci., 155 (2020) 106412.
[26] H. Ma, Z. Duan, X. Ning, L. Su, Numerical investigation on heat transfer behavior of thermally developing flow inside rectangular microchannels, Case Stud. Therm. Eng., 24 (2021) 100856.
[27] A. Bejan, E. Sciubba, The optimal spacing of parallel plates cooled by forced convection, Int. J. Heat Mass Transf., 35(12) (1992) 3259-3264.
[28] A. Mohanty, R. Das, Laminar flow in the entrance region of a parallel plate channel, AIChE Journal, 28(5) (1982) 830-833.
[29] A. Bejan, Convection heat transfer, John Wiley & Sons, 2013.
[30] R.K. Shah, A.L. London, Laminar flow forced convection in ducts: a source book for compact heat exchanger analytical data, Academic press, 2014.
[31] S.W. Churchill, H. Ozoe, Correlations for laminar forced convection in flow over an isothermal flat plate and in developing and fully developed flow in an isothermal tube, (1973).
[32] R.W. Hornbeck, An all-numerical method for heat transfer in the inlet of a tube, in: Mechanical Engineering, ASME-Amer Soc Mechanical Eng 345 E 47TH ST, New YORK, NY 10017, 1966, pp. 76.
[33] R. Manohar, Analysis of laminar-flow heat transfer in the entrance region of circular tubes, Int. J. Heat Mass Transf., 12(1) (1969) 15-22.
[34] G. Hwang, S. Ja-Pung, Effect of radial velocity component on laminar forced convection in entrance region of a circular tube, Int. J. Heat Mass Transf., 17(2) (1974) 372-375.
[35] J.P. Hartnett, T.F. Irvine, G.A. Greene, Y.I. Cho, Advances in heat transfer, Academic press, 1998.
[36] F. Kreith, R.M. Manglik, M.S. Bohn, Principles of heat transfer, Cengage learning, 2012.

[37] R.L. Webb, Performance evaluation criteria for use of enhanced heat transfer surfaces in heat exchanger design, Int. J. Heat Mass Transf., 24(4) (1981) 715-726.
[38] H. Nemati, M. Moghimi, P. Sapin, C. Markides, Shape optimisation of air-cooled finned-tube heat exchangers, Int. J. Therm. Sci., 150 (2020) 106233.
[39] H. Nemati, A. Rahimzadeh, C.-C. Wang, Heat transfer simulation of annular elliptical fin-and-tube heat exchanger by transition SST model, J. Cent. South Univ., 27(8) (2020) 2324-2337.
[40] H. Nemati, S. Samivand, Numerical study of flow over annular elliptical finned tube heat exchangers, Arab J. Sci. Eng., 41(11) (2016) 4625-4634.
[41] A. Bejan, Advanced engineering thermodynamics, John Wiley & Sons, 2016.

Appendix I

It is known that for a fully developed flow:

$$\overline{Nu} = \frac{1}{4\,Z^{*}} \ln\left(\frac{T_{\mathrm{w}} - T_{\infty}}{T_{\mathrm{w}} - T_{\mathrm{m}}}\right) \tag{I1}$$

for a distance far enough from the duct inlet, the effect of the entrance region on $\overline{Nu}$ is negligible and therefore:

$$Nu = \lim_{Z^{*}\to\infty} \overline{Nu} \tag{I2}$$

However, for a known $q"$:

$$q" = h_{\infty}(T_{\mathrm{w}} - T_{\infty}) = h(T_{\mathrm{w}} - T_{m}) \Rightarrow \frac{h_{\infty}}{h} = \frac{Nu_{\infty}}{Nu} = \frac{T_{\mathrm{w}} - T_{\mathrm{m}}}{T_{\mathrm{w}} - T_{\infty}} \\ = \exp\,(-4Nu\,Z^{*}) \tag{I3}$$

For a rectangular channel, $Nu = 2.976$ [30]. So:

$$Nu = \lim_{Z^{*}\to\infty} \exp(-4 \times 2.976\,Z^{*}) = \lim_{Z^{*}\to\infty} \exp(-11.904\,Z^{*}) \tag{I4}$$